ARL-TR-9001 ● JULY 2020

DEVCOM ARMY RESEARCH LABORATORY

Exploring the Feasibility of Using Cryomilled Aluminum Powder as Feedstock for Laser Powder Bed Fusion Additive Manufacturing

by Frank Kellogg, John Derek Demaree, and Brandon McWilliams

NOTICES

Disclaimers

The findings in this report are not to be construed as an official Department of the Army position unless so designated by other authorized documents.

Citation of manufacturer's or trade names does not constitute an official endorsement or approval of the use thereof.

Destroy this report when it is no longer needed. Do not return it to the originator.

ARL-TR-9001 ● JULY 2020

Exploring the Feasibility of Using Cryomilled Aluminum Powder as Feedstock for Laser Powder Bed Fusion Additive Manufacturing

Frank Kellogg
SURVICE Engineering

John Derek Demaree and Brandon McWilliams
Weapons and Materials Research Directorate, CCDC Army Research Laboratory

REPORT DOCUMENTATION PAGE

Form Approved
OMB No. 0704-0188

1. REPORT DATE *(DD-MM-YYYY)*	2. REPORT TYPE	3. DATES COVERED (From - To)
July 2020	Technical Report	1 May 2019–1 March 2020

4. TITLE AND SUBTITLE
Exploring the Feasibility of Using Cryomilled Aluminum Powder as Feedstock for Laser Powder Bed Fusion Additive Manufacturing

5a. CONTRACT NUMBER
W911QX-16-D-0014

5b. GRANT NUMBER

5c. PROGRAM ELEMENT NUMBER

6. AUTHOR(S)
Frank Kellogg, John Derek Demaree, and Brandon McWilliams

5d. PROJECT NUMBER

5e. TASK NUMBER

5f. WORK UNIT NUMBER

7. PERFORMING ORGANIZATION NAME(S) AND ADDRESS(ES)
CCDC Army Research Laboratory
ATTN: FCDD-RLW-MD
Aberdeen Proving Ground, MD 21005

8. PERFORMING ORGANIZATION REPORT NUMBER
ARL-TR-9001

9. SPONSORING/MONITORING AGENCY NAME(S) AND ADDRESS(ES)

10. SPONSOR/MONITOR'S ACRONYM(S)

11. SPONSOR/MONITOR'S REPORT NUMBER(S)

12. DISTRIBUTION/AVAILABILITY STATEMENT
Approved for public release; distribution is unlimited.

13. SUPPLEMENTARY NOTES
ORCID IDs: Frank Kellogg, 0000-0003-3048-0255; John Derek Demaree, 0000-0001-8244-4761

14. ABSTRACT
Aluminum alloy 5083 (AA5083) is an attractive candidate for many Army applications due to its high strength and corrosion resistance. The continuing development of additive manufacturing (AM) techniques enables design and/or material changes to legacy parts, can contribute to the Army's efforts to manufacture lightweight vehicles and equipment, and helps drive interest in using parts made from high-strength aluminum (Al) alloys produced by powder-based AM. However, most Al alloys that are of interest for their mechanical properties, including AA5083, experience hot cracking during AM processes that makes these alloys unusable in most laser-based AM processes (such as laser powder bed fusion [LPBF]). Current research has shown that one way to overcome hot cracking issues is by making changes to the chemical composition of the Al alloys, such as adding zirconium (Zr) or scandium (Sc) to AA5083. Alternatively, cryomilling AA5083 powder may be an alternative method to improve the performance of AA5083 during LPBF without the time and cost increases associated with alloy development. Cryomilling has been shown to lead to the incorporation of dissolved nitrogen and Al nitride as a solid solution within the Al matrix. These additions may behave like Zr or Sc and help alleviate the hot cracking issues during LPBF. In this study, as-atomized AA5083 powder was cryomilled in liquid nitrogen and welded with a laser to physically simulate the LPBF process. Changes in the powder morphology and chemistry from the cryomilling process led to powders that proved more weldable than the as-atomized powder and suggest feasibility for improved performance as a feedstock material for LPBF.

15. SUBJECT TERMS
cryomilling, additive manufacturing, laser powder bed fusion, powder feedstock, aluminum alloy 5083

16. SECURITY CLASSIFICATION OF:			17. LIMITATION OF ABSTRACT	18. NUMBER OF PAGES	19a. NAME OF RESPONSIBLE PERSON
a. REPORT	b. ABSTRACT	c. THIS PAGE			Frank Kellogg
Unclassified	Unclassified	Unclassified	UU	40	19b. TELEPHONE NUMBER (Include area code) (410) 306-0803

Contents

List of Figures

List of Tables

Acknowledgments

Special thanks to Dr Clara Mock for the X-ray microcomputed tomography analysis and her help during the cryomilling experiments.

Special thanks to Dr Matthew Dunstan for the use of his equipment during these experiments.

The research reported in this document was performed in connection with contract/instrument W911QX-16-D-0014 with the US Army Combat Capabilities Development Command (CCDC) Army Research Laboratory. The views and conclusions contained in this document are those of SURVICE Engineering and the CCDC Army Research Laboratory. Citation of manufacturer's or trade names does not constitute an official endorsement or approval of the use thereof. The US Government is authorized to reproduce and distribute reprints for Government purposes notwithstanding any copyright notation hereon.

1. Introduction

Laser powder bed fusion (LPBF) is an additive manufacturing (AM) technique by which parts are produced layer by layer using a laser to weld metal powder particles together.[1,2] This layer-by-layer approach allows for much more freedom in part design than is available from more traditional manufacturing pathways. The downside to the LPBF process is that it works best with alloys that are easily cast, which can dramatically limit the number of alloys available for LPBF. Among aluminum (Al) alloys, only simple Al-silicon (Si) (4XXX series alloys) with near eutectic chemistries ($AlSi_{12}$, $AlSi_{10}Mg$) are widely used in AM LPBF.[1,2] High-strength Al alloys, including Al alloy 5083 (AA5083), exhibit hot cracking and tearing during the LPBF process, making it impossible to use these materials as feedstocks.[1–3] Hot cracking can be addressed through small alterations to the alloy chemistry, such as adding small amounts of scandium (Sc) or zirconium (Zr) to act as grain nucleation sites.[3] However, these changes to the alloy compositions increase the cost of the material and are subject to availability issues due to supply chain disruptions. In this study, rather than changing alloy composition through direct alloying additions, cryomilling was explored as a method to promote the formation of nucleation particles and reduce the crack sensitivity of AA5083 to make it a suitable feedstock for producing dense and crack-free parts with LPBF.

Cryomilling is attrition ball milling of powder either at cryogenic temperatures or within cryogenic liquid (argon or nitrogen). For this study, cryomilling refers to powder milling in liquid nitrogen. Cryomilling in liquid cryogen is a relatively low-energy milling process that can yield micron-sized powders with nanostructured grains. Milling under liquid nitrogen has also been shown to lead to the incorporation of nitrogen into solid solution with Al as well as the formation of Al nitride (AlN).[4–6] AlN has been shown to behave as a grain pinner and may behave like Sc or Zr additions.[3–6] Previous research has also shown that cryomilled AA5083 sinters to full density at lower temperatures than as-atomized AA5083 and obtains a higher hardness.[4–6] This study examined whether the improved sinterability of cryomilled AA5083 can help with the processibility of AA5083 powder during LPBF.

2. Experimental

Each cryomill run consisted of 1 kg of as-atomized AA5083 powder, previously sieved with a –325 mesh screen, mixed with 0.15 wt% graphite. The graphite and AA5083 were mixed in two 500-g batches using a LabRAM II acoustic mixer at a setting of 10 g's of acceleration for 1 h, after which the two batches were combined.

Graphite is introduced as a hydrogen-free process control agent (PCA) to prevent excessive cold welding during cryomilling.[4]

Cryomilling was done using an attritor mill with 1/4-inch-diameter stainless steel (440C) milling media with a 32:1 ratio between media and powder. Each cryomill run started by allowing the mill to fill with liquid nitrogen and then adding 50 g of AA5083 powder (no graphite) as a coating run. This allows the mill vessel and media to be coated with sacrificial powder and leads to increased yields with decreased contamination. Each coating run lasted for 30 min, after which the liquid nitrogen powder slurry was discharged. The mill was then refilled with liquid nitrogen before adding the 1-kg powder batches. Three runs were performed, with powders being milled for 2, 4, or 8 h. After discharge, the liquid nitrogen powder slurry was collected in a large steel bucket and placed in a glovebox to allow the excess liquid nitrogen to boil off under argon to prevent oxidation. The powder was collected and weighed in the glovebox with each run yielding between 830 and 870 g of powder. From each run, 250 g was taken for degassing. To identify any extra changes solely due to the degassing process, 250 g of the as-atomized powder was also degassed.

Degassing is the process of heat treating the powders to drive off any surface impurities that may have been introduced during the milling process.[4–6] These powders were degassed in a fluidized bed rocking furnace developed for the US Army Combat Capabilities Development Command (CCDC) Army Research Laboratory by MATSYS, Inc. (Herndon, Virginia). The powder was loaded, and sealed, in a reactor inside the glovebox under argon before being loaded into a rocking furnace. The powders were heated under flowing argon for 6 h at 350 °C and then furnace cooled overnight before being unloaded and collected inside the glovebox.

Each powder was characterized for morphology (scanning electron microscopy [SEM] and Camsizer [Camsizer X2 Particle Size and Shape Analyzer from Retsch Technology]), particle size (Camsizer), flow (Brookfield Powder Flow Tester), phase and grain size determination (X-ray diffraction [XRD]), and surface chemistry (Rutherford backscattering spectrometry [RBS]).

The LPBF process was simulated using an IPG Photonics laser welder (1070 nm ytterbium quartz laser). The advantages of the laser welder were that very small sample sizes could be used and that cleanup was easy with no chance of contamination. The disadvantages were that the laser welder does not offer control over the same process parameters as commercial LPBF machines, primarily powder layer thickness control and beam diameter. Powder layer thickness in these experiments was 2 mm. This value is normally less than 100 μm during LPBF.[1,2,7]

The laser welder has a beam size of 375 μm compared to beam diameters of 3–5 μm found in most AM processes.[1,2,7]

To reproduce the build environment in an LPBF machine, the powders were loaded into a special airtight vessel (designed and built by Matt Dunstan, CCDC Army Research Laboratory, Fig. 1) inside the glovebox to ensure an inert, argon, atmosphere during laser welding.[8] The top of the vessel included an IR transparent window to allow for laser welding without breaking atmospheric control (Fig. 1D). The powders were put into a 12- by 12- by 2-mm deep well on a metal tray (Fig 1B) that was loaded into the airtight vessel (Fig. 1C).

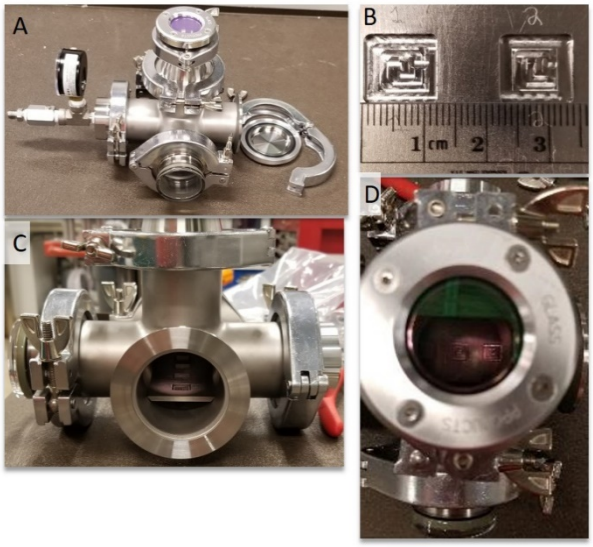

Fig. 1 Powder containment vessel, showing A) the vessel, B) the sample tray and powder wells, C) the sample tray loaded into the vessel, and D) the view through the IR transparent window.

The as-atomized powder was laser welded using different laser traverse speeds and powers to determine optimal laser parameters for use with the other samples. Sample quality was determined by weld bead uniformity and fragility documented via photography, optical microscopy, and X-ray microcomputed tomography (μCT). XRD was used to determine if there were any phase changes after welding and whether any nanostructuring imparted during cryomilling survived the welding process. The as-cryomilled powders were examined using RBS with a 2.0-MeV He+ ion beam from a tandem positive ion accelerator (National Electrostatics model 5SDH-2) and a backscattering angle of 175° to estimate the composition and thickness of the oxides on the surface of the powders. The spectra were analyzed using the SIMNRA program (www.simnra.com; M. Mayer at Max-Planck-Institut für Plasmaphysik).

3. Results and Discussion

3.1 Laser Welding

Laser welding with the as-atomized AA5083 powder was initially done at 50-W beam power over multiple laser traverse speeds (5, 25, 50, 100, and 150 mm/s) to determine optimal laser traverse speeds. A left-to-right snake-type raster pattern was used with a 1-mm distance between traverses (this is analogous to hatch spacing in LPBF, Fig. 2F). The presence of cracks, uniformity in bead structure, and fragility of the sample were determined by optical photography and microscopy (Figs. 2 and 3).

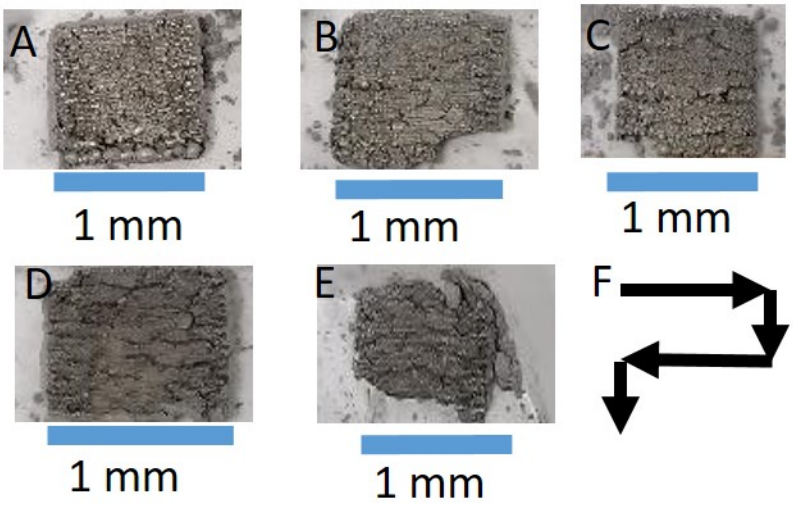

Fig. 2 As-atomized powder laser welded at 50 W and traverse speeds of A) 5, B) 25, C) 50, D) 100, and E) 50 mm/s. F is a schematic of the raster pattern.

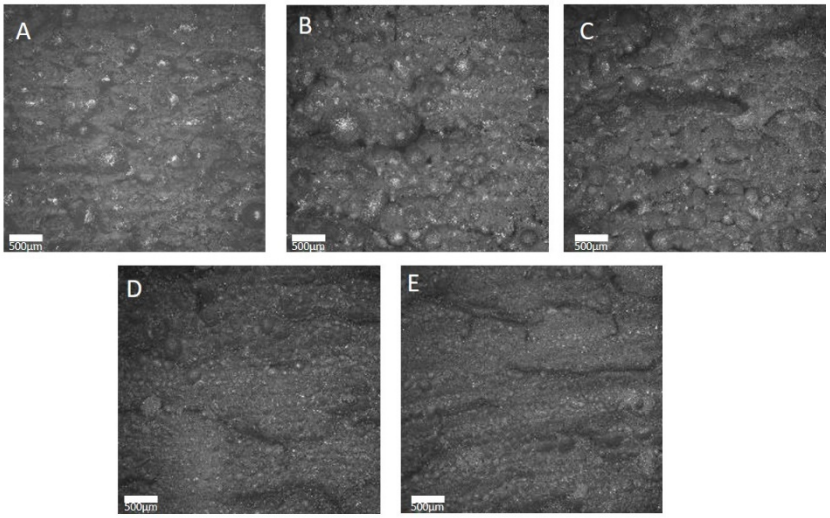

Fig. 3 Optical microscopy images of the as-atomized powder laser welded at 50 W and traverse speeds of A) 5, B) 25, C) 50, D) 100, and E) 150 mm/s

All of these samples show extensive hot cracking, as seen in the literature when using as-atomized, non-weldable, Al alloy powders.[1–3] It was also observed that, at slower traverse speeds, more powder was blown around the test vessel. During the LPBF process, each layer should be a continuous weld bead. When there is not enough energy imparted to the powder bed, surface tension effects cause the bead to break and solidify as discrete pieces (this process is called balling and is detrimental to part properties).[1,2] While sample A in Figs. 2 and 3 shows the least amount of the cracking, the large amount of balling, along with the amount of powder blown away from the sample well, was judged to be too detrimental for further experimentation at 5 mm/s traverse speed. Besides sample A, sample D in Figs. 2 and 3 shows the least cracking, does not exhibit a lot of powder being blown around during welding, and also appears to have more uniform balling, indicating some process improvement. Based on these observations of sample D, 100 mm/s was judged to be the optimal laser traverse speed. Laser welding of the as-atomized powder was then repeated at laser powers of 75 and 100 W at 100 mm/s traverse speed to determine the best power level (Fig. 4). Of these, the sample produced at 50 W and 100 mm/s (Fig. 4A and 4D) was the best sample, as increasing the laser wattage led to larger balling and more cracking.

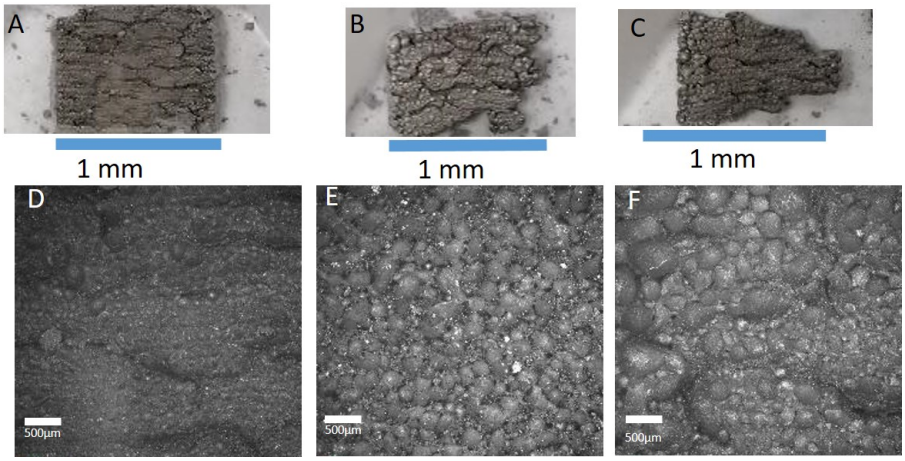

Fig. 4 Pictures and optical microscopy images of as-atomized powder laser welded at a traverse speed of 100 mm/s at 50 W (A and D), 75 W (B and E), and 100 W (C and F)

With degassed as-atomized powder (Fig. 5), the sample welded at 50 W and 100 mm/s had more cracking than when the as-atomized powder was used (Fig. 5A and 5C). The degassed powder welded at 100 W had less cracking than at 50 W but more balling (Fig. 5B and 5D). Overall, it was observed that lower traverse speeds led to samples with less cracking but with larger and more varied balling. Increases in beam power seem to lead to samples with both more cracking and larger balling. The degassed powder showed an increase in balling with beam power but a decrease in cracking relative to the non-degassed powder. In all samples, the largest balling was observed around the edges of the sample (left, right, top, and bottom). This most likely occurs because the powder on the edges of the sample corresponds to the ends of the raster pattern and experiences the most time under the laser beam.

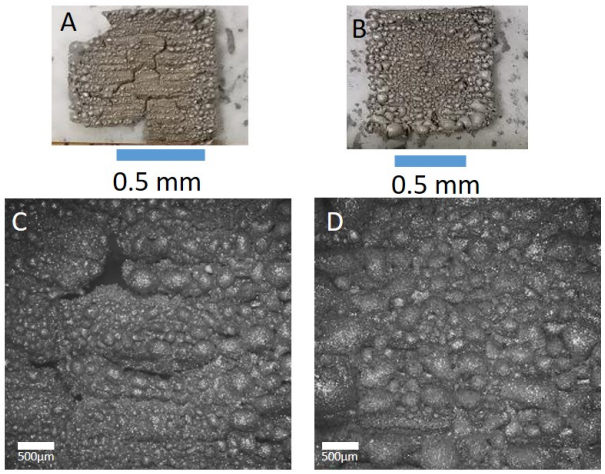

Fig. 5 Pictures and optical microscopy images of as-atomized powder degassed at 350 °C and laser welded at a traverse speed of 100 mm/s at 50 W (A and C) and 100 W (B and D). The scale in A and B is in millimeters.

With the 2-h cryomilled powder, the samples welded under the laser showed little to no cracking and less balling. At 50-W beam power it was observed that large, but uniform, balling was produced at low traverse speeds (25 mm/s, Fig. 6A and 6D). Balling appears to be the smallest in the sample produced at 100 mm/s (Fig. 6B and 6E), while at 150 mm/s the balling appears to be larger than at 100 mm/s but smaller than at 50 mm/s (Fig. 6C and 6F). There are also some pores present that were not seen at the lower traverse speeds.

At a traverse speed of 100 mm/s, increasing beam power from 50 to 100 W led to an increase in balling without inducing any crack or pore formation (Fig. 7). Based on an overall decrease in cracking, it is clear the 2-h cryomilled powder outperformed the as-atomized powders, with the 50-W 100 mm/s sample being judged the best based on a lack of cracks or pores and having the most uniform bead structure.

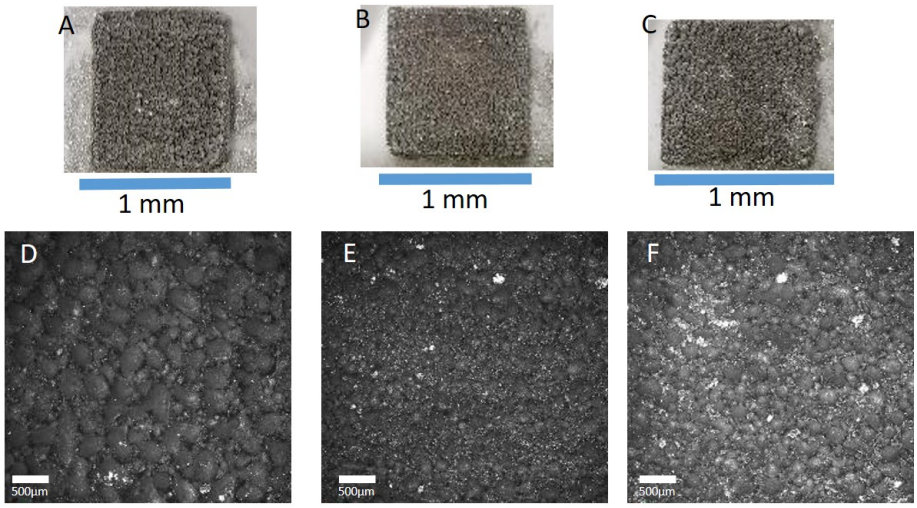

Fig. 6 Pictures and optical microscopy images of 2-h cryomilled powder laser welded at 50 W and 25 (A and D), 100 (B and E), and 150 mm/s (C and F) laser traverse speeds

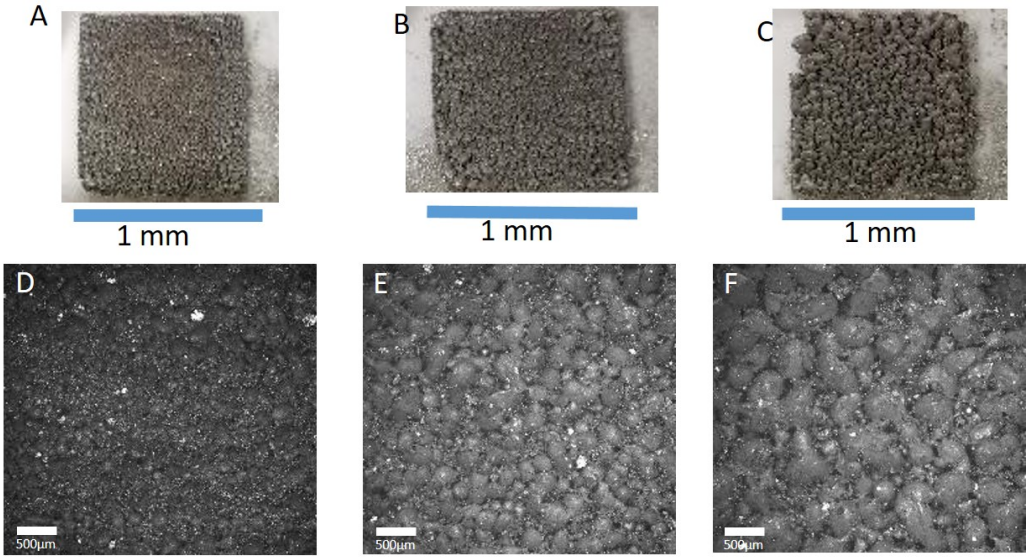

Fig. 7 Pictures and optical microscopy images of 2-h cryomilled powder laser welded at 100 mm/s traverse speed and 50- (A and D), 75- (B and E), and 100-W (C and F) beam powers

After degassing, the 2-h cryomilled powder did not exhibit the same degree of weldability as before degassing. The best results for the 2-h cryomilled and degassed powder were produced at 100 mm/s and 50 W, as this sample had relatively small balling and no obvious pores or cracks (Fig. 8B and 8E). There were obvious pores when welded at 50 W and 25 mm/s (Fig. 8A and 8D) and hot cracking at 50 W and 150 mm/s and (Fig. 8C and 8F). When welded at 100 mm/s and 100 W, the sample produced from this degassed powder had larger balling than

at 50 W but no obvious pores or cracks (Fig. 9B and 9D). Based on the presence of porosity, cracking, and balling, it is apparent that the 2-h cryomilled and degassed powder did not weld as well under the laser as the 2-h cryomilled powder, although it still welded better than the as-atomized powder.

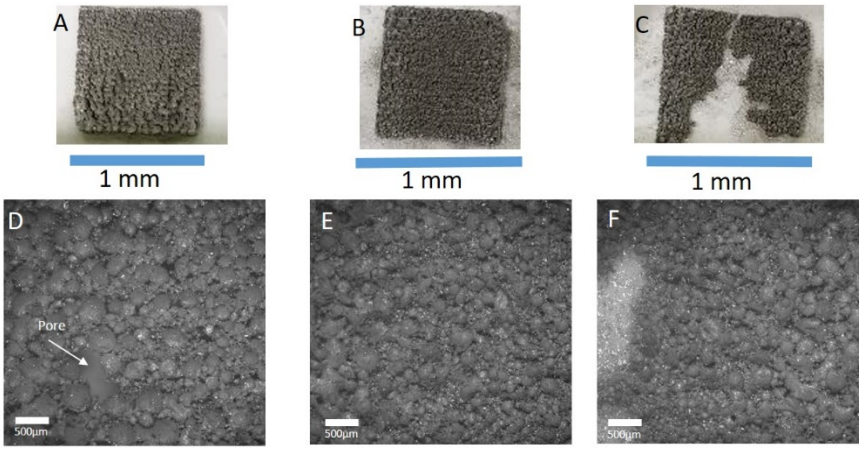

Fig. 8 Pictures and optical microscopy images of 2-h cryomilled powder degassed at 350 °C for 6 h and laser welded at 50 W and 25 (A and D), 100 (B and E), and 150 mm/s (C and F) laser traverse speeds

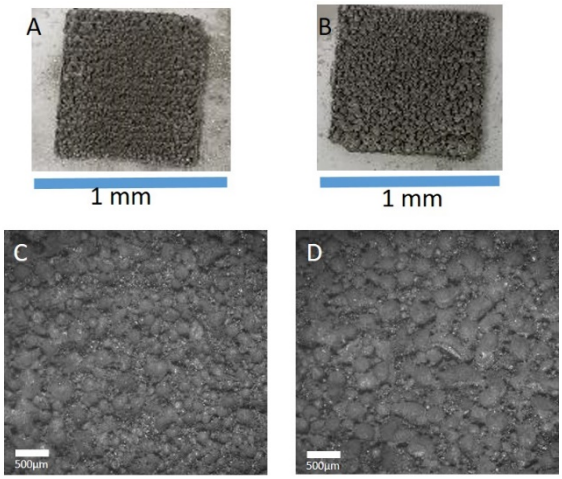

Fig. 9 Pictures and optical microscopy images of 2-h cryomilled powder degassed at 350 °C and laser welded at a traverse speed of 100 mm/s at 50 W (A and C) and 100 W (B and D)

Since the best results have been achieved when the powders are welded at 50 W and 100 mm/s traverse speed, the 4-h cryomilled powder was only laser welded under these conditions (Fig. 10) while the 4-h cryomilled and degassed powder was laser welded at 100 mm/s and both 50 and 100 W (Fig. 11). There appears to be little noticeable difference between the 4- and 2-h cryomilled powders after laser

welding. The 4-h cryomilled and degassed powder produced samples that cracked after welding at a power level of 50 W, meaning it is less weldable than the powder that was degassed after cryomilling for 2 h. Like the previous powders, 50 W and 100 mm/s laser parameters provided the best results for both versions of the 4-h cryomilled powder.

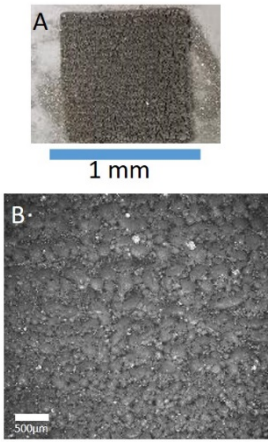

Fig. 10 Pictures and optical microscopy images (A and B) of 4-h cryomilled power laser welded at 50 W and 100 mm/s traverse speed

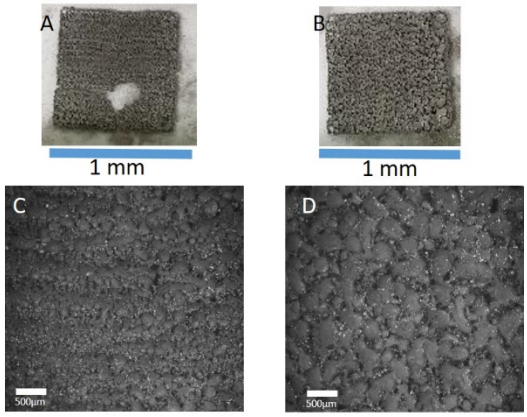

Fig. 11 Pictures and optical microscopy images of 4-h cryomilled powder degassed at 350 °C for 6 h and laser welded at 100 mm/s and 50 (A and C) and 100 W (B and D)

Figures 12 and 13 show the results of laser welding powder that had been cryomilled for 8 h, with and without degassing, respectively. These samples were thicker than any of the previous samples and appear to be the best welded samples produced during these experiments. The pictures and images for 8-h cryomilled sample show very little differences between samples made with a 100 mm/s traverse speed at either 50 or 100 W (Fig. 12). The 8-h cryomilled and degassed sample appears to show finer and more uniform beads than the previous degassed

samples, with the 50 W sample producing more uniform beads and better results than the 100 W sample (both were welded with a traverse speed of 100 mm/s) (Fig. 13).

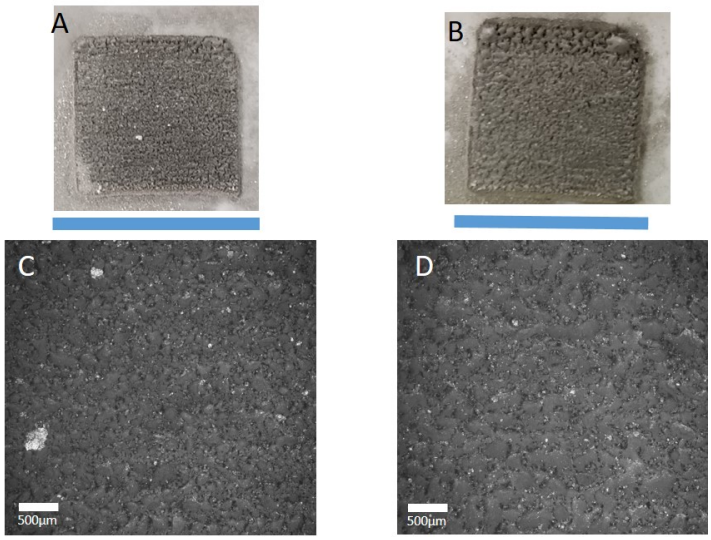

Fig. 12 Pictures and optical microscopy images of 8-h cryomilled power laser welded at 100 mm/s traverse speed and 50- (A and C) and 100-W (B and D) beam powers

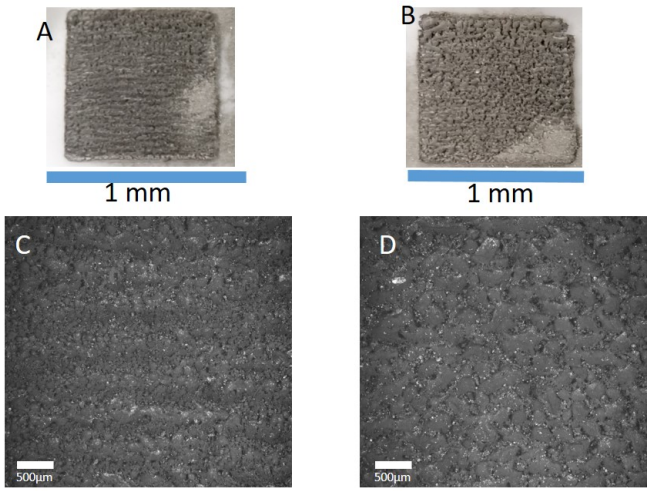

Fig. 13 Pictures and optical microscopy images of 8-h cryomilled powder degassed at 350 °C for 6 h and laser welded at 100 mm/s and 50 (A and C) and 100 W (B and D)

A 3-D view of the welded samples was sought to get a complete picture of how well the powders were welding together. A Zeiss Xradia 520 Versa µCT unit (at 40 kV, 1-s exposure time, 4× optical magnification with a 3.5-µm pixel size) was used to image welded samples on the top, bottom, and through the cross section of

the sample. Because of sample fragility only two samples were examined, the 2-h cryomilled sample produced at 50 W and 100 mm/s traverse speed and the 8-h cryomilled sample welded at 100 W and 100 mm/s (Fig. 14). The µCT images show some pores in the 2-h cryomilled sample (Fig. 14A, 14B, and 14C) that were not readily observed from the sample pictures or optical microscopy images (Fig.7A and 7D). The µCT images also show that the beads made during laser welding are not present throughout the cross section (Fig. 14C) indicating that the laser was only melting the top (approximate) 250 µm of the powder bed while the back of the sample (the bottom of the powder bed) is poorly welded powder with no signs of melting or consolidation (Fig. 14B and 14C). The µCT images for the 8-h cryomilled sample show no signs of porosity and an increased thickness of almost double that of the 2-h sample (Fig. 14D, 14E, and 14F), although it is also poorly consolidated beneath the top layer (Fig. 14E and 14F). This is not completely unexpected as in this attempt to simulate the LPBF process, the powder bed depth/layer thickness is 2 mm while in actual LPBF the layer thickness is much smaller (less than 100 µm). The improved laser weldability of the 8-h cryomilled relative to all of the other powder samples examined is clearly defined in the images (Fig. 12) and µCT images (Fig. 14).

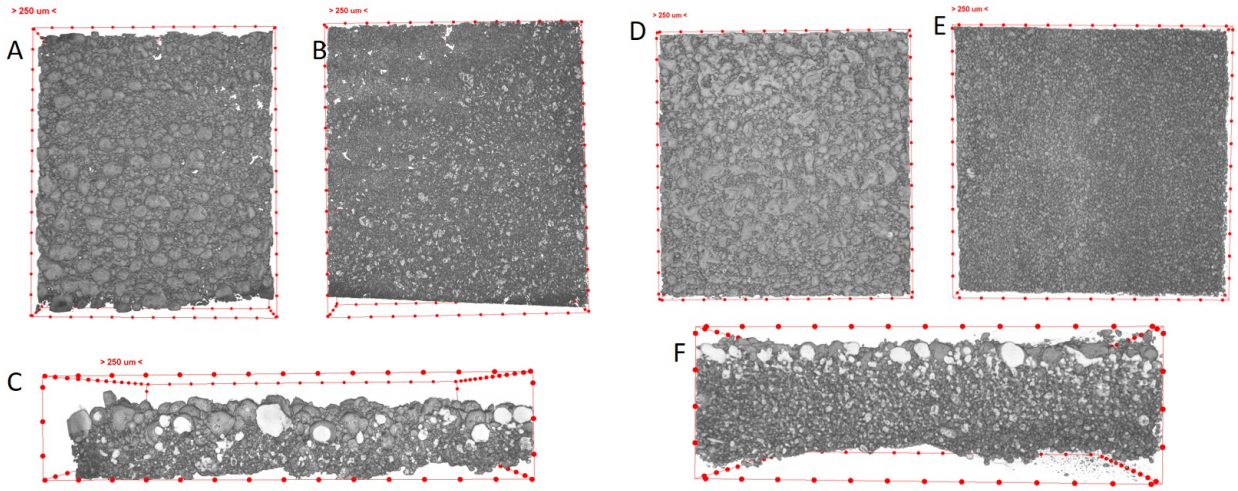

Fig. 14 A) Top, B) bottom, and C) side views of the 2-h cryomilled sample laser welded at 50 W and 100 mm/s traverse speed taken via µCT. The scale distance between each red circle is 250 µm.

While the cryomilled powder has shown improved laser weldability, it needs to be verified that the welded samples are still viable. AA5083 is not heat treatable due to its propensity to form intermetallic compounds (typically Al_yMn_x) upon heating. XRD was used to determine whether the AA5083 powders could be laser welded without developing these intermetallic phases.

The XRD results show (Figs. 15–19; all XRD data generated for these experiments was with a Co X-ray source) that during laser welding, the intermetallic phase readily forms (Figs. 18 and 19) along with a possible spinel (MgAlO) phase (all powder diffraction file [PDF] cards referenced in the figures are from the International Centre for Diffraction Data [ICDD] XRD database version 4.2001). These phases were not present in the as-atomized powder (Fig. 15) or the as-cryomilled powders (Fig. 16), but they may have been present in the degassed powders (Fig. 17). Figures 15 and 16 illustrate how, during cryomilling, there were no phase changes detected and no contaminants introduced in percentages large enough for XRD to measure. This is not surprising, as even after 8 h of cryomilling, new phases can be present in very small amounts; for instance, AlN formed from nitrogen incorporation has been measured as approximately 2 $\times 10^{-2}$ volume percent.[6] The broadened peaks, relative to the peaks for the as-atomized material, in Fig. 16 indicate that the cryomilling process has produced nanostructured powders.[4–6, 9–12] Figure 17 reveals that the degassed powders have retained the nanostructuring of the as-cryomilled powders. The small peaks between 45°and 53° 2-theta in Fig. 17 were identified as intermetallic phase(s).

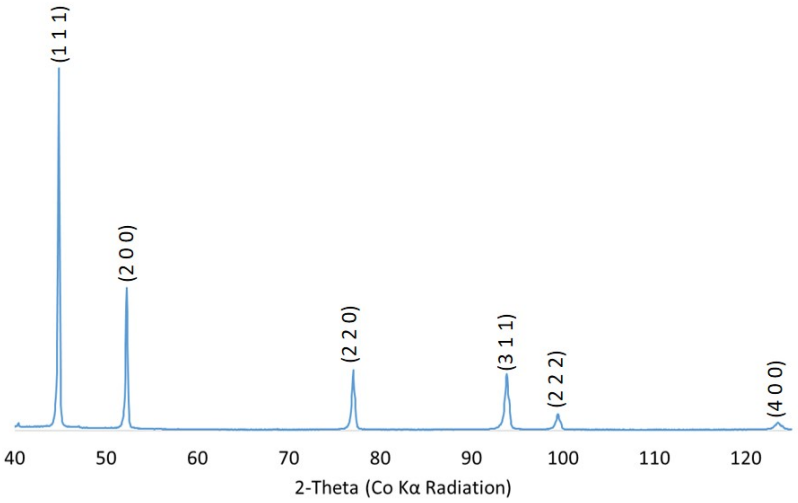

Fig. 15 XRD pattern for as-received AA5083 powder. Peaks identified from XRD ICCD PDF Card 00-04-0787 (star pattern for Al) under Co Kα radiation (λ=17.8896 nm).

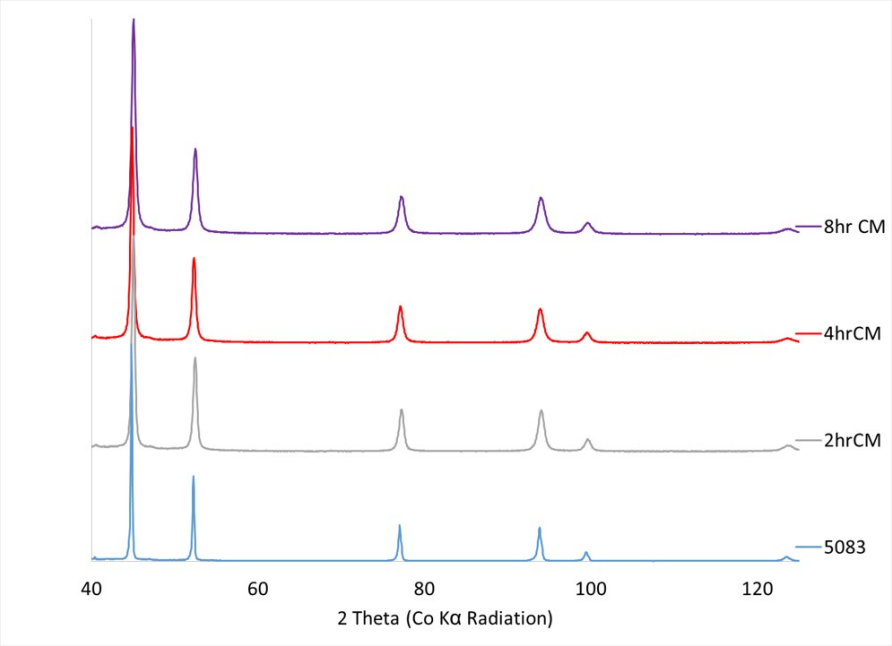

Fig. 16 XRD patterns for AA5083 powder and as-cryomilled powders at 2, 4, and 8 h. Notes: CM = cryomilled; hr = hour.

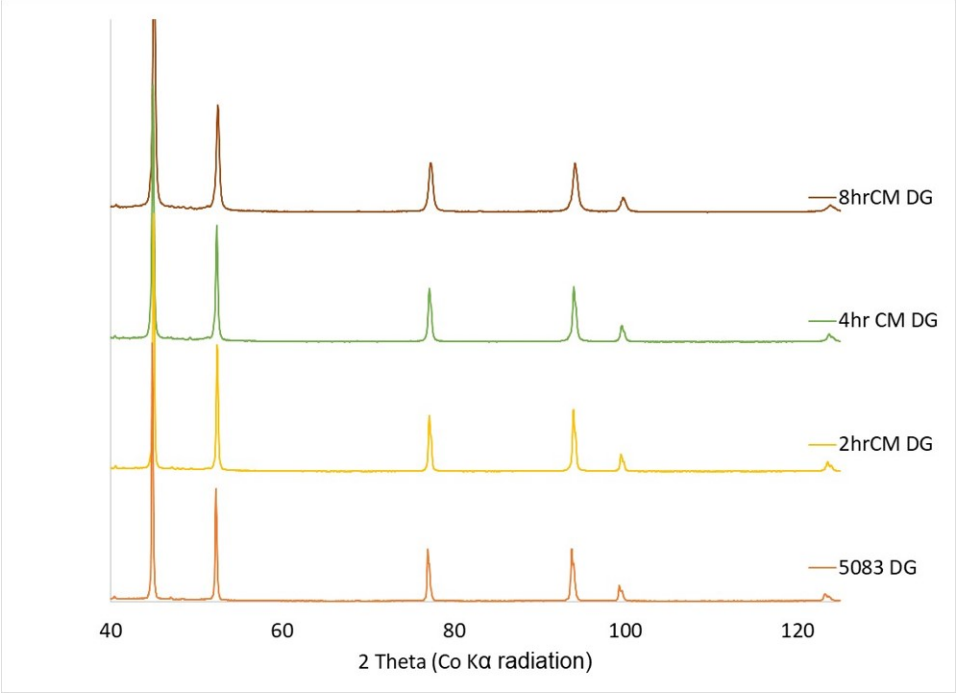

Fig. 17 XRD patterns for AA5083 powder and cryomilled powders at 2, 4, and 8 h after degassing. Notes: CM = cryomilled; DG = degassing; hr = hour.

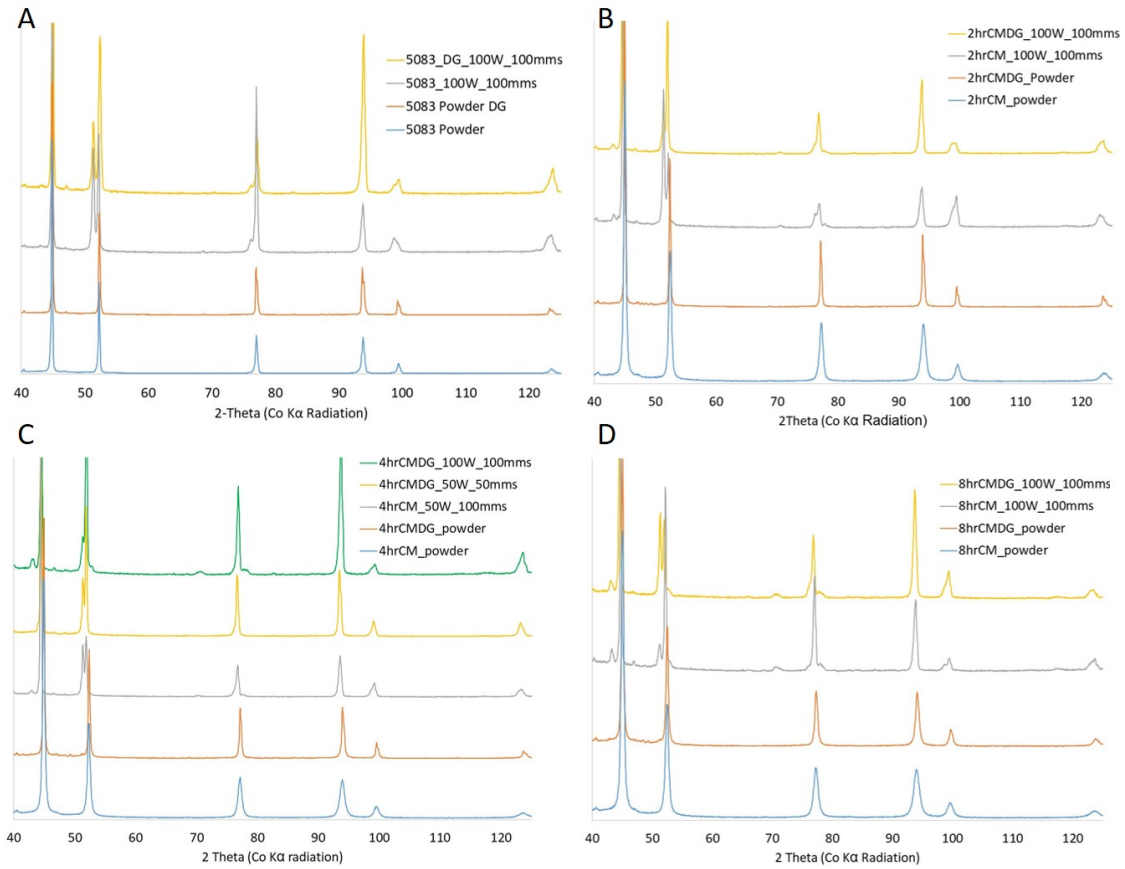

Fig. 18 XRD patterns of AA5083 (A), 2-, 4-, and 8-h cryomilled samples (B, C, and D) comparing powders to laser-welded samples

Peak Label	2 Theta (°)	Material/PDF Card	Plane/PDF Card Intensity
1	43.72	Spinel(Mg0.734Al2.177O4)/04-009-7708	(3 1 1)/1000
2	46.95	Al11Mn4.6/01-078-3033	(3 0 5) 17M
3	50.84	Al11Mn4.6/01-078-3033	(3 5 2)(5 3 3)*/1000M
4	70.62	Spinel(Mg0.734Al2.177O4)/04-009-7708	(5 1 1)/399
5	77.95	Spinel(Mg0.734Al2.177O4)/04-009-7708	(4 4 0)/634

* Both hkl indices are listed at the 2 theta position on the PDF card as the most intense (100%) peak.

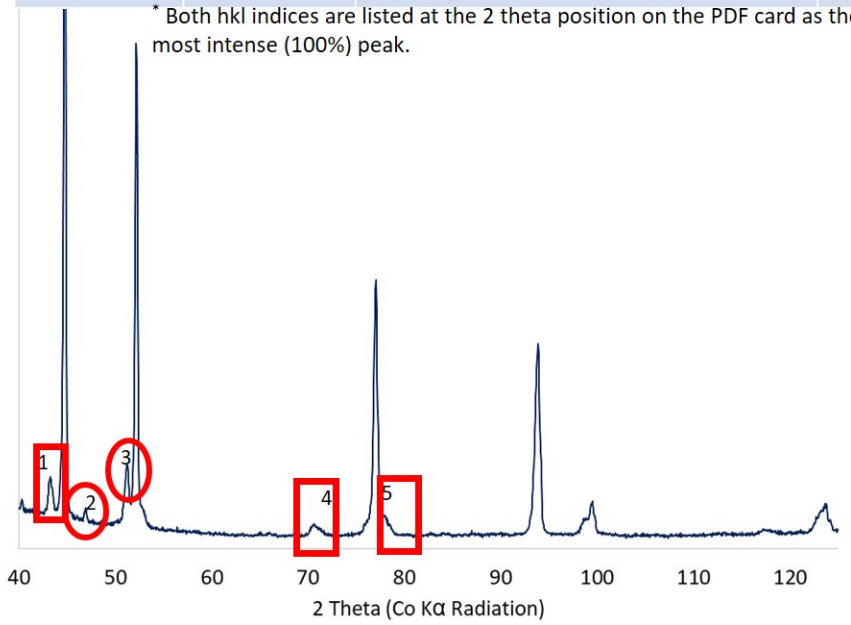

Fig. 19 XRD pattern for 8-h cryomilled powder laser welded at 100 W and 100 mm/s used to illustrate different phases found after welding

The intermetallic peaks are much more prominent after laser welding (Figs. 18 and 19). While the intermetallic phase is known to form during the heat treatment of AA5083, the spinel phase (AlMgO, Figs. 18 and 19) is unexpected. It may be possible that during laser welding, the vapor pressure differences between Al and magnesium (Mg) (they have similar melting temperatures but Mg has a much lower boiling point and is known to have issues with vaporization during AM LPBF[1–3]) may have led to spinel forming due to reactions between the Mg dissolved in solid solution within the Al matrix and any oxygen that may have been present in either the powder or test chamber.

Both crystallite size and the percentage of each phase present can be calculated from the XRD spectra by curve fitting the peaks and comparing them to standard peak shape and position[9–12] (Table 1). In this study, Bruker's TOPAS software was used to do the peak fitting via a Rietveld analysis using a double Voigt approach and a Gaussian fit for each peak (assuming a first principles peak type).[11,12]

Table 1 Crystallite size calculations for cryomilled powders

Powder	Crystallite size (nm)	Strain	Goodness of fit
2-h CM	28.8 ± 1.0	$3.10 \times 10^{-4} \pm 1.8 \times 10^{-3}$	2.41
2-h CMDG	86.7 ± 1.7	$2.53 \times 10^{-4} \pm 1.0 \times 10^{-4}$	2.32
4-h CM	56.0 ± 0.9	$1.66 \times 10^{-3} \pm 7.0 \times 10^{-4}$	1.37
4-h CMDG	70.8 ± 4.5	$6.40 \times 10^{-4} \pm 3.0 \times 10^{-4}$	2.47
8-h CM	22.10 ± 0.5	$2.28 \times 10^{-3} \pm 4.0 \times 10^{-4}$	2.02
8-h CMDG	29.4 ± 0.5	$1.15 \times 10^{-3} \pm 3.0 \times 10^{-4}$	2.50

Notes: CM = cryomilled; CM DG = cryomilled and degassed

For crystallite size, the peak broadening phenomenon only occurs when the average grain size of the material is less than 100 nm (the measured grain size via transmission electron microscopy [TEM] for the as-atomized powder is 0.2 to 2 μm).[9–13] The goodness of fit (GOF) for each calculation is included to illustrate how well TOPAS was able to fit the X-ray data and to provide a rough idea of the accuracy of the calculations. A GOF of 1 indicates a perfect fit, while anything under 4 is considered acceptable.[11,12] Despite all of the GOF values in the table indicating a good fit, the calculated crystallite sizes for the 2-h cryomilled samples seem to be very small relative to the milling time and need TEM examination for verification. The calculated crystallite size for the 8-h cryomilled samples matches well with previous results[4–6] that were directly measured via TEM analysis.

After laser welding, the crystallite calculations were all above 100 nm. While a crystallite size could not be accurately obtained from XRD analysis, the measurements do show that the powder's nanostructuring was not retained during laser welding.

From Figs. 18 and 19, it is clear that the laser-welding process led to the formation of phases, in addition to the intermetallic phases, that were not present in any of the powder samples. Upon fitting these data, it was possible to calculate weight percentages of each phase (Table 2). The rough sample surfaces, combined with the similar stoichiometry of each peak, made proper fitting of the XRD spectra more difficult than experienced with the powder samples. Given these sample limitations, along with general limitations of XRD calculations, it was not surprising to see poor GOF values and relatively large standard deviations in the calculations. Further examination using a TEM to verify the phases present is warranted.

Table 2 Weight percentages of phases calculated from XRD data after laser welding

Sample/power (W)/speed (mm/s)	Wt% Al	Wt% $Mg_{0.05}Al_{0.95}$	Wt% $Mg0_{.08}Al_{0.92}$	Wt% $Mg_{0.13}Al_{0.87}$	Wt% $Al_{0.44}Mn_{0.56}$	Wt% $Al_{0.87}Mn_{0.13}$	Wt% $Al_{11}Mn_{4.6}$	Wt% Spinel ($Mg_{0.734}Al_{2.177}O_4$)	GOF
AA5083/100/100	84 ± 3	5.6 ± 1.5	…	…	11 ± 3	…	…	0 ± 0	2.56
AA5083DG/100 /100	14 ± 2	78 ± 2.0	…	…	8.2 ± 1.5	…	…	0 ± 0	3.15
2-h CM/100/100	0.0 ± 1.3	83 ± 3.0	…	…	13 ± 2.0	…	…	4 ± 2.0	2.54
2-h CMDG/100/100	0.0 ± 1.8	…	97 ± 5.0	…	0 ± 4.0	[a]	…	3 ± 3.0	3.73
4-h CM/50/100	10 ± 2.0	…	…	80±5.0	3 ± 2.0	…	…	7 ± 4.0	2.36
4-h CMDG/50/50	14 ± 0.5	…	…	72±1.0	5 ± 9.0	[a]	…	9 ± 7.0	2.97
4-h CMDG/100/100	12 ± 1.6	…	79 ± 2.0	…	7.5 ± 1.3	[a]	…	1.6 ± 1.3	3.06
8-h CM/100/100	0.5 ± 0.4	88.4 ± 1.7	…	…	…	…	8.1 ± 1.6	3.0 ± 7.0	2.35
8-h CMDG/100/100	4.9 ± 1.2	1.5 ± 1.2	75 ± 3.0	…	12 ± 2.0	…	…	7 ± 2.0	2.94

[a] Indicates that while the phase was detected, the PDF card did not provide the data necessary for calculating weight percentage present.

In addition to the Al-manganese (Mn) intermetallic and the spinel phase mentioned previously, several different Al_xMg_y phases were also identified. While Mn is known to leave solid solution with Al upon welding AA5083, Mg generally does not.[4–6] The formation of the Al-Mg phases could be driven by the rapid melting and solidification of the powder under the laser not allowing time for Mg to dissolve back into the Al matrix or by the vaporization of Mg under the laser. Some evidence for this may be gleamed from the fact that the Al-Mg and Al-Mn phases that formed were influenced by the powder and laser parameters used (Table 2).

Three different Al-Mn phases were used to identify peaks in the XRD data. With the exception of the 8-h cryomilled sample, all of the laser-welded samples appear to have the $Mn_{0.56}Al_{0.44}$ phase present. After degassing, the 2- and 4-h cryomilled samples also had $Al_{0.87}Mn_{0.13}$, while the 8-h cryomilled sample only had $Al_{11}Mn_{4.6}$ present. It is hard to derive a pattern from the data to determine what links there are between the powder, processing parameters, and formation of the Al-Mn phases. These samples do not include the Al_6Mn phase previously seen upon heat treating cryomilled AA5083,[4,6] which is probably attributable to differences in thermal profiles experienced by the powders in each.

Three different Al-Mg phases were also detected. $Mg_{0.13}Al_{0.87}$ was only found in the samples welded with a beam power of 50 W (using either 4-h cryomilled or a 4-h cryomilled and degassed powder). $Mg_{0.08}Al_{0.92}$ was found in all of the samples made with cryomilled-degassed powder welded at a beam powder of 100 W. The

as-atomized and the cryomilled powders welded with a beam power of 100 W had the $Mg_{0.05}Al_{0.95}$ phase present, and only the sample made with the 8-h cryomilled and degassed powder had multiple Al-Mg phases present as both $Mg_{0.08}Al_{0.92}$ and $Mg_{0.05}Al_{0.95}$ were found (the calculations show that $Mg_{0.05}Al_{0.95}$ is only present in very small amounts, 1.5%, with a large standard deviation of ±1.2%, casting doubt on whether this phase is actually present). It appears that processing parameters can drive which Al-Mg phase forms. Laser power, as seen with the different 4-h cryomilled samples, appears to affect which phases are present. Cryomilling combined with degassing also appear to drive which phases form as the as-atomized and degassed powder was the only degassed powder that did not form $Mg_{0.08}Al_{0.92}$ when laser welded. Beam power and whether the powder was degassed appear to play large roles in determining which Al-Mg phases are present.

When the cryomilled powders are laser welded, a spinel phase ($Mg_{0.734}Al_{2.177}O_4$) also forms in small amounts. The analysis of this phase is made difficult because its presence is based on one peak in each spectrum being identified as spinel. Even though this peak is present in all of the samples made with cryomilled powder, and it is the 100% intensity peak for the identified spinel phase, phase identification and quantification are not reliable based off a single peak. The calculations reflect this with the large standard deviations listed in Table 2 with the spinel weight percentages. In light of the issues just discussed, it does appear that degassing decreases the amount of spinel present (with the exception of the 8-h cryomilled powders, as the standard deviation in the calculations for the 8-h as-cryomilled powder is especially large). This seems to indicate that the driving force for spinel formation is oxygen picked up during cryomilling. Since the degassed powders tended to weld worse than the non-degassed powders, the spinel phase may be acting like Sc or Zr additions.[3]

3.2. Powder Characterization

When working with cryomilled powders, the first observed change in the powder is that it flows much more readily than the as-atomized powder. The as-atomized AA5083 powder does not flow very well and often clogged the funnels used to transfer the powder into the mill. After cryomilling, the powder was free flowing and did not clog any funnels during transfer. Powder rheometry (Brookfield powder flow tester) was used to quantify these observations (Fig. 20). Powder rheometry takes a known mass and volume of powder and imparts a shear load on the powder bed and measures the force needed to make a powder bed collapse and move. The relationship between the unconfined failure strength of the powder bed (the force needed to make a powder bed collapse) and the major principal consolidating stress

(the load needed to make loose powder into a free-standing powder bed) is plotted to provide a general idea of how well the powder flows.

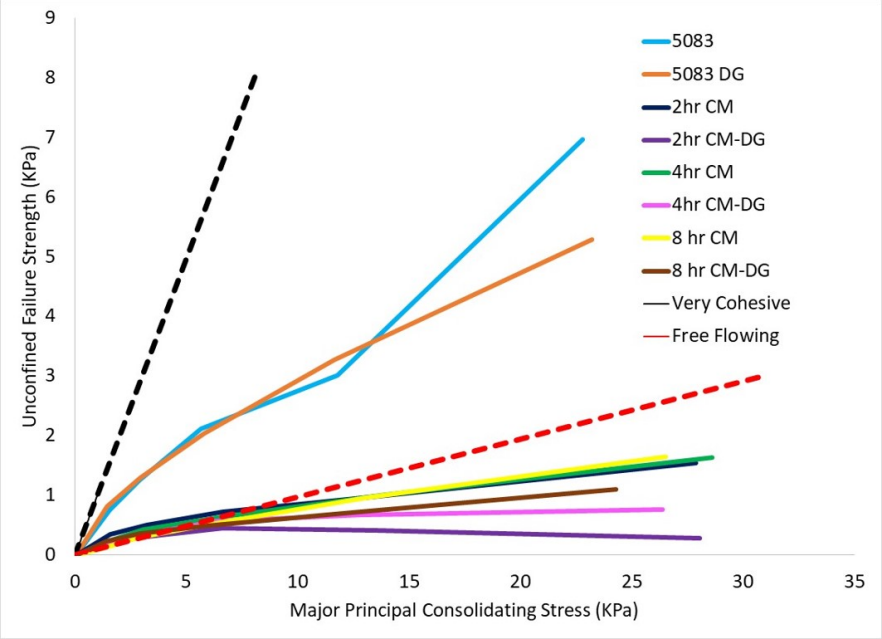

Fig. 20 Brookfield powder flow measurements for the as-atomized (AA5083), cryomilled, and degassed powders. The black and red dashed lines are included as reference data considered cohesive and free-flowing powders, respectively. Notes: CM = cryomilled; DG = degassed.

Powder flow data can be evaluated by comparing the measured and reference flow behavior for cohesive (non-flowing) and free-flowing powders shown in Fig. 20. The results show that the as-atomized powder is closer to cohesive than free-flowing and that degassing helps improve flow, most likely through the removal of moisture and hydroxide groups absorbed during cryomilling.[6,14] All of the cryomilled powders are free-flowing and there is no difference with regard to milling time in powder flow. However, the degassed cryomilled powders were the most free-flowing. However, the degassed powders show slight decreases in flow with increased milling time. Powder flow is generally controlled by powder morphology, size and distribution, and surface chemistry.[14–16] All of these characteristics are changed during cryomilling.

SEM examinations of the powders (Figs. 21 and 22) show that the sphericity of the as-atomized powder was lost after cryomilling. Powder cryomilled after 2 and 4 h produced plate-shaped particles with large length-to-thickness aspect ratios (Fig. 21C, 21D, 21E, and 21F). After 8 h of cryomilling, the powder is no longer plate shaped and instead is more equiaxed with an aspect ratio closer to the as-atomized powder than the shorter milling time powders (Fig. 21G and 21H). The

decreased aspect ratio of the 8-h cryomilled powders allows this powder to pack better than the 2- or 4-h cryomilled samples and helps improve the weldability of the powder.[17] The decreased aspect ratio may also reduce laser reflectivity as a further aid to weldability.

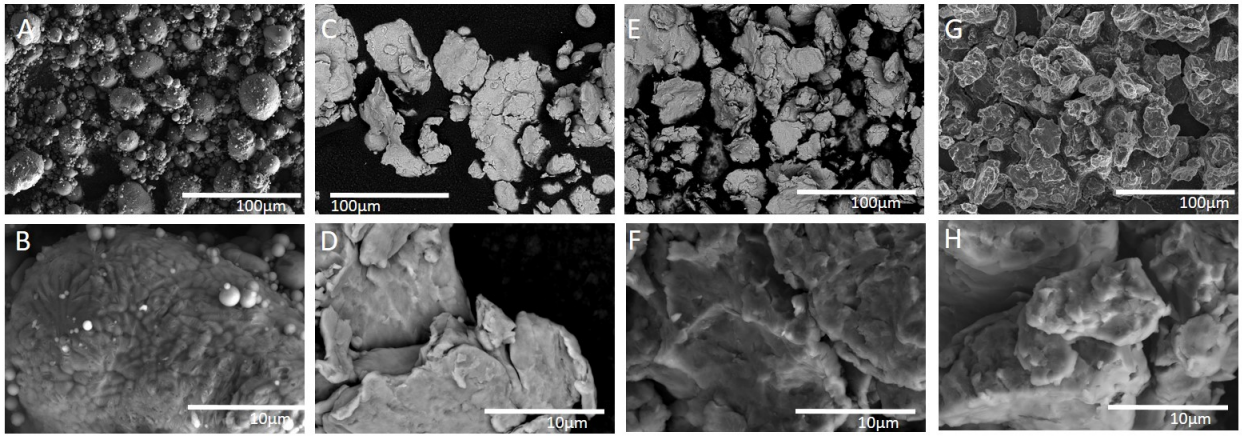

Fig. 21 SEM images comparing the particle morphology of the as-received (A and B), 2- (C and D), 4- (E and F), and 8-h (G and H) cryomilled powders (images C–F are backscattered electrons [BSEs] and all others are secondary electrons [SEs])

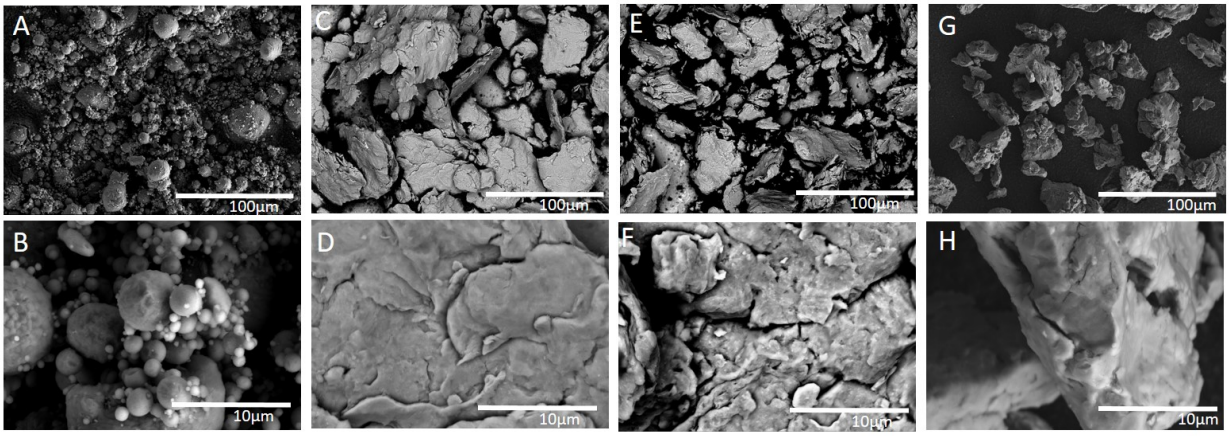

Fig. 22 SEM images comparing the particle morphology of the degassed powders in the as-received (A and B), 2- (C and D), 4- (E and F), and 8-h (G and H) cryomilled states (images C–F are BSE all others are SE)

While Fig. 22 shows that the degassing process had no influence on particle morphology, both Figs. 21 and 22 show that the finest particles and the satellite particles seen in the as-atomized powder (the A and B images in Figs. 21 and 22) are no longer present after cryomilling. The disappearance of both the fines and the satellite particles leads to improved powder flow.[14–16] The changes observed in particle morphology with milling time and particle size were quantified using the Camsizer X-2.

The Camsizer uses two high-speed cameras at different magnifications to capture images of particles in freefall. From these images, the Camsizer can quantify various particle characteristics such as sphericity (Fig. 23 and Table 3), symmetry, and particle size distribution (PSD) (Fig. 24 and Table 3).[18] The Camsizer does not appear to do a good job capturing the morphological changes as the calculated changes to symmetry and sphericity (Fig. 23, Table 2) do not appear to properly indicate the severity of the changes seen in the SEM (Figs. 21 and 22). This occurs because the 2- and 4-h cryomilled powders have such exaggerated aspect ratios, that particles falling past the cameras on edge will not be captured (the thickness of the particles is less than the 1–2 µm resolution of the cameras), while particles falling with the large surface facing the camera are measured as roughly symmetrical spheres.

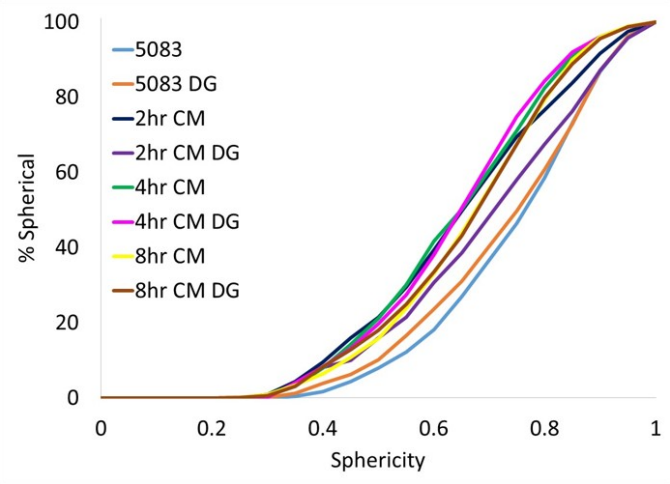

Fig. 23 Sphericity measurements for the as-atomized (AA5083), cryomilled, and degassed powders. Notes: CM = cryomilled; DG = degassed.

Table 3 PSD and morphology values

Powder	D10 (µm)	D50 (µm)	D90 (µm)	Mean value sphericity	Mean value symmetry
AA5083	4.92	14.31	28.18	0.74	0.90
5083 DG	4.90	14.29	28.35	0.73	0.90
2-h CM	16.21	40.45	102.07	0.65	0.89
2-h CM DG	17.00	41.87	106.17	0.69	0.89
4-h CM	16.87	31.58	62.48	0.64	0.90
4-h CM DG	17.25	32.01	62.32	0.64	0.89
8-h CM	17.83	32.59	62.48	0.66	0.90
8-h CM DG	18.43	33.81	65.66	0.66	0.90

Notes: CM = cryomilled; CM DG = cryomilled and degassed.

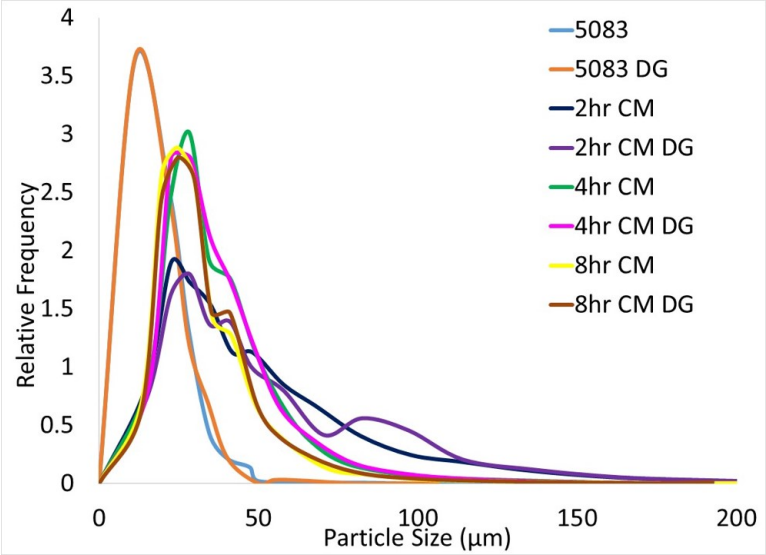

Fig. 24 PSD curves for the as-atomized (AA5083), cryomilled, and degassed powders. Notes: CM = cryomilled; CM DG = cryomilled and degassed.

The measured PSD (Fig. 24, Table 3) values correlate well with what is observed in the SEM images. Because the as-atomized powder was sieved with a –325 mesh (particles larger than 45 µm were removed), the non-cryomilled powders have the narrowest PSD curves (Fig. 24) and the smallest measured sizes (Table 3). During cryomilling, particles are initially cold welded and begin to agglomerate (even when using a PCA); hence the loss of fines during cryomilling and increases in the D10, D50, and D90 values. As milling time increases, these agglomerates start to break back down into smaller particles, hence the decrease in D50 and D90 values after 4 h of cryomilling. The removal of fines and satellites, as observed through the SEM images and PSD measurements, is the reason for the improved flow of the cryomilled powders.

Throughout the experiments, degassing improves powder flow without affecting particle size or morphology. Degassing has been shown to remove chemical species accumulated during cryomilling, primarily organic species containing H, O, and OH groups.[6] The removal of these species may be why the degassed powder has improved flow. The reason that flow decreases after degassing with increased milling time may be indicative of incomplete degassing. While the loss of particle sphericity would normally be expected to lead to a decrease in particle flow, the loss of the finest particles, removal of satellites, and removal of surface impurities are possible mechanisms for improved particle flow.

In addition to the absorbed organic groups removed by degassing, it is theorized that the cryomilling process can change the nature of the oxide layer present on Al particles.[4–6] Changes to the oxide layer may explain why cryomilled Al powder

laser welds better than the as-atomized powder. RBS was used to examine the surface oxide layers of the Al powder to determine if there were any surface chemistries not related to the absorbed organic species.[19]

There were difficulties generating clean RBS results. The precision of the layer thickness measurements was limited because the samples were powders that do not have smooth and flat surfaces (smooth, flat surfaces are best for controlling scattering). Additionally, since oxygen is a smaller atom than Al, the differences in the ion scattering radii make it difficult to accurately quantify the amount of oxygen present.

The RBS measurements still showed a decrease in oxide layer thickness with milling time (Figs. 25 and 26).

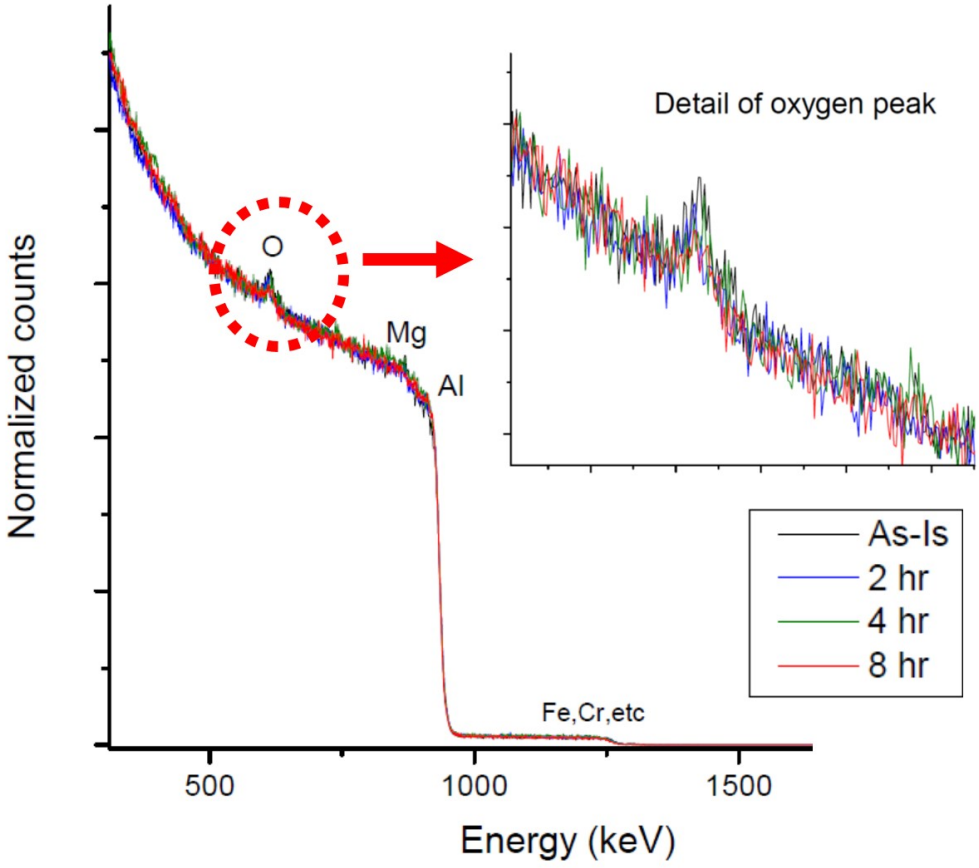

Fig. 25 RBS measurements comparing the as-atomized powder to the 2-, 4-, and 8-h as-cryomilled powders. The inset labeled "Detail of oxygen peak" shows that the oxide layer thickness for the 8-h powder is much less than that of the as-atomized powder.

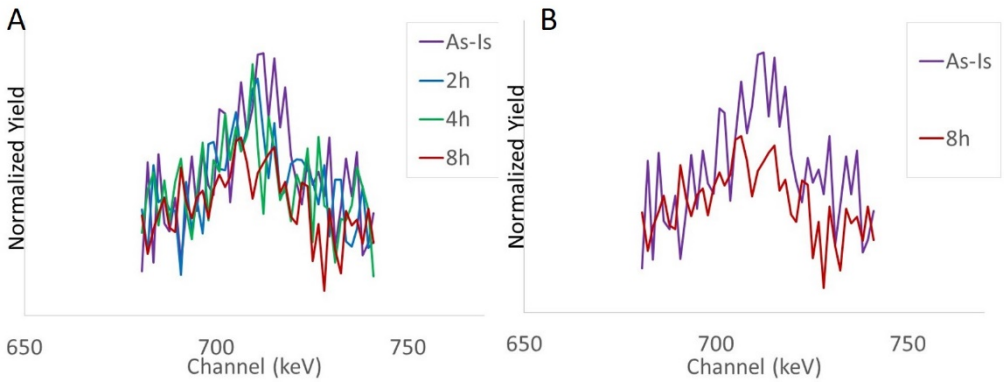

Fig. 26 The RBS oxygen peak: A) all of the powders together; B) the differences between the as-atomized and 8-h cryomilled powders

Layer thicknesses were measured by comparing the area under the oxygen peak for each powder measured. The as-atomized powder had the largest oxygen peak (Fig. 26). Taking the area under the curve for the as-atomized powder as 100%, it was found that the areas under the oxygen peaks for the 8-h as-cryomilled powders were roughly 45% of the as-atomized peaks. With the oxide layer around the as-atomized powders measured at roughly 15 nm, this puts the oxide layer for the 8-h as-cryomilled powder at roughly 7 to 8 nm, roughly half as thick as the as-atomized powder. Figure 26 shows that it was very hard to discern differences between the as-atomized powder and the 2- and 4-h cryomilled samples.

It has been shown here and elsewhere that at least 8 h of cryomilling are needed to completely nanostructure AA5083 and to improve sinterability.[4–6] The results for the 2- and 4-h samples may be reflections of this and may be indicative of incomplete milling. It is pure speculation, but it may be possible that the oxide layer must be significantly broken down prior to achieving sufficient cryomilling. These changes in the oxide layer do not affect flow, as seen in Fig. 20.

4. Conclusions

Cryomilled AA5083 exhibits better laser welding than as-atomized AA5083. The hot cracking that occurs when trying to use AA5083 in laser-based AM has its root cause in the extremely rapid melting and solidification encountered during laser welding. It has been shown that the addition of alloying elements, such as Zr or Sc, can solve the hot cracking issue by providing nucleation sites for finer grain growth.[3] Cryomilling in liquid nitrogen has been shown to dissolve nitrogen within the Al matrix as well as lead to the formation of AlN, which behaves as a grain pinner.[4–6] These changes to the Al matrix may behave much like the additions of Zr or Sc and may be the reason cryomilled AA5083 appears to be less prone to

cracking during laser welding than as-atomized AA5083. However, the creation of AlN and uptakes of dissolved nitrogen have previously been shown to need at least 8 h of cryomilling and cannot account for the increased weldability after 2 and 4 h of cryomilling.[4–6] The improved weldability of the 2- and 4-h cryomilled powder may be linked to the formation of a spinel phase during laser welding that behaves similarly to the Zr or Sc additions in Zhou et al.[3] While the oxide layer may not have been reduced enough after 4 h of cryomilling, it was after 8 h and, along with a decrease in the aspect ratio, may be why the 8-h cryomilled powder showed the best weldability.

While the cryomilled powders have improved flow and laser welding relative to the as-atomized powder, the XRD results indicate that Mg is no longer in a solid solution with Al. Since AA5083 gets its strength from forming a solid solution with Mg, the formation of these phases may be detrimental to the final mechanical properties of any AM builds using cryomilled AA5083 as a feedstock. While it looks like some Mg left the solid solution in Zhou et al.,[3] they did not report the different phases found in this study. This suggests that it may be possible to suppress the formation of unwanted Al-Mg phases through laser processing parameter optimization.

This study has shown that the laser welding of AA5083 can be improved by using cryomilled powders, albeit while raising questions about the final chemistry of a built part. The next steps would be to see how these improvements translate to welding using a laser with closer parameters to an LPBF AM machine and determine whether cryomilled AA5083 can be used to produce a 3-D dimensional part for further microstructural and mechanical property analysis.

5. References

1. Aboulkhair N, Simonelli M, Parry L, Ashcroft I, Tuck C, Hague R. 3-D printing of aluminum alloys: additive manufacturing of aluminium alloys using selective laser melting. Progress in Materials Science. 2019;106:1–45. https://doi.org/10.1016/j.pmatsci.2019.100578.

2. Aversa A, Marchese G, Saboori A, Bassini E, Manfredi D, Biamino S, Ugues D, Fino P, Lombardi M. New aluminum alloys specifically designed for laser powder bed fusion: a review. Materials. 2019;12:1007. https://doi.org/10.3390/ma12071007.

3. Zhou L, Hyer H, Park S, Pan H, Bai Y, Rice K, Sohn Y. Microstructure and mechanical properties of Zr-modified aluminum alloy 5083 manufactured by laser powder bed fusion. Additive Manufacturing. 2019;28:485–496. https://doi.org/10.1016/j.addma.2019.05.027.

4. Kellogg F, Hofmeister C, Giri A, Cho K. Nanostructuring of aluminum alloy powders by cryogenic attrition with hydrogen-free process control agent. Aberdeen Proving Ground (MD): Army Research Laboratory (US); 2015 Feb. Report No.: ARL-TR-7208.

5. Kellogg F, McWilliams B, Sietins J, Giri A, Cho K. Comparison of SPS processing behavior between as atomized and cryomilled aluminum alloy 5083 powder. Metallurgical and Materials Transactions A. 2017;48a:5492–5499. doi: 10.1007/s11661-017-4286-4.

6. Hofmeister C, Zhou L, Kellogg F, Giri A, Cho K, Sohn Y. Effects of degassing on the microstructure, chemistry, and estimated mechanical properties of a cryomilled Al-Mg Alloy. Metallurgical and Materials Transactions A. 2018; 49(7):3066–3079. https://doi.org/10.1007/s11661-018-4627-y.

7. DebRoy T, Wei H, Zuback J, Mukherjee T, Elmer J, Milewski J, Beese A, Wilson-Heid A, De A, Zhang W. Additive manufacturing of metallic components – process, structure and properties. Progress in Materials Science. 2018;92:112-224. https://doi.org/10.1016/j.pmatsci.2017.10.001.

8. Dunstan M. CCDC Army Research Laboratory, Aberdeen Proving Ground, MD, unpublished data.

9. Zhang Z, Zhou F, Lavernia E. On the analysis of grain size in bulk nanocrystalline materials via X-ray diffraction. Metallurgical and Materials Transactions A. 2003;34:1349–1355.

10. Dorofeev G, Streletskii A, Povstugar I, Protasov A, Elsukov E. Determination of nanoparticle sizes by X-ray diffraction. Colloid Journal. 2012;74(6):675–685. doi: 10.1134/S1061933X12060051.

11. Lutteroitti L. Introduction to Rietveld refinements. Class notes. [accessed 2020 Mar 23]. https://www.researchgate.net/post/How_can_I_improve_the_peak_shape_fitting_in_Rietveld_refinements_using_TOPAS_software via: http://www.xray.cz/xray/csca/kol2011/kurs/Dalsi-cteni/Luca-Lutterotii-Rietveld.pdf.

12. Speakman S. Precision and accuracy, agreement indices in HSP, class notes. [accessed 2020 Mar 26]. http://prism.mit.edu/xray/oldsite/RietveldGOF.pdf via: http://prism.mit.edu/xray/oldsite/tutorials.htm.

13. Yao B, Hofmeister C, Patterson T, Sohn Y, Van Den Bergh M, Delahanty T, Cho K. Microstructural features influencing the strength of trimodal aluminum metal-matrix-composites. Composites: Part A. 2010;41:933–941. doi:10.1016/j.compositesa.2010.02.013.

14. Goh H, Heng P, Liew C. Comparative evaluation of powder flow parameters with reference to particle size and shape. International Journal of Pharmaceutics. 2018;547:133–141. https://doi.org/10.1016/j.ijpharm.2018.05.059.

15. Bumiller M. The importance of particle shape. Technical note. [accessed 2020 Mar 23]. https://www.horiba.com/scientific/products/particle-characterization/download-center/webinars/tr017/.

16. Leturia M, Benali M, Lagarde S, Ronga I, Saleh K. Characterization of flow properties of cohesive powders: a comparative study of traditional and new testing methods. Powder Technology. 2014;253:406–423. doi: http://dx.doi.org/10.1016/j.powtec.2013.11.045.

17. German R. Particle packing characteristics. Princeton (NJ): Metal Powder Industries Federation; 1999.

18. Understanding the shape parameters reported by the CAMSIZER. Horiba Technical Note 164 (TN164). [accessed 2020 Apr 16]. https://www.horiba.com/scientific/products/particle-characterization/download-center/technical-notes/ on 4/16/2020.

19. Krieger U, Huthwelker T, Daniel C, Weers U, Peter T, Landford W. Rutherford backscattering to study the near-surface region of volatile liquids and solids. Science. 2002;295(5557):1048–1050. doi: 10.1126/science.1066654.

List of Symbols, Abbreviations, and Acronyms

3-D	three-dimensional
AA5083	aluminum alloy 5083
Al	aluminum
AlN	aluminum nitride
AM	additive manufacturing
BSE	backscattered electron
CCDC	US Army Combat Capabilities Development Command
CM	cryomilled
Co	cobalt
DG	degassed
GOF	goodness of fit
ICDD	International Centre for Diffraction Data
IR	infrared
LPBF	laser powder bed fusion
Mg	magnesium
Mn	manganese
PCA	process control agent
PDF	powder diffraction file
PSD	particle size distribution
RBS	Rutherford backscattering spectrometry
Sc	scandium
SE	secondary electron
SEM	scanning electron microscopy
Si	silicon
TEM	transmission electron microscopy

XRD	X-ray diffraction
Zr	zirconium
μCT	X-ray microcomputed tomography

1 (PDF) DEFENSE TECHNICAL INFORMATION CTR DTIC OCA

1 (PDF) CCDC ARL FCDD RLD CL TECH LIB

6 (PDF) CCDC ARL FCDD RLW D B MCWILLIAMS FCDD RLW MD F KELLOGG A KUDZAL C MOCK K CHO FCCD RLW MF J DEMAREE